International Journal of Environmental Sciences
ISSN: 2229-7359
Vol. 11 No. 21s, 2025
https://theaspd.com/index.php

Structural, Thermal, And Electrochemical Insights Into $Znfe_2O_4$ Nanoparticles Synthesized Via Co-Precipitation

Jaba Sherin. S[1], Maria Lenin.M[2,5], S.R. Gibin[3], R. Gopalakrishnan[4]
[1]Research Scholar, Department of Physics, Annai Velankanni College, Tholayavattam, Kanyakumari District -629157, Tamil Nadu, India.
[2]Associate Professor, Department of Physics, Annai Velankanni College, Tholayavattam, Kanyakumari District – 629157, Tamil Nadu, India
[3]Associate Professor of Physics, Sree Sakthi Engineering College (Autonomous), Karamadai, Coimbatore-641104, Tamil Nadu, India
[4]Assistant Professor of Physics, Sri Ranganathar Institute of engineering and technology Coimbatore - 641110, Tamil Nadu, India
[5]Manonmaniam Sundaranar University, Abishekapatti-627012, Tirunelveli, Tamil Nadu, India.
*Corresponding author: Dr. Maria Lenin.M (E-mail: ria.lenin@gmail.com)

Abstract
In this work, $ZnFe_2O_4$ nanoparticles were successfully synthesised by a simple, high yield and low-cost co-precipitation method. The $ZnFe_2O_4$ nanoparticles were fully characterized by X-ray diffraction analysis (XRD), scanning electron microscope (SEM) with (EDX), Fourier transform infrared spectroscopy (FTIR) and thermal analysis (TG/DTA). XRD and FTIR analyses reveal that the synthesized $ZnFe_2O_4$ nanoparticles were of phase pure with cubic structure. Morphological study of FESEM images reveals that the particles were in quasi-cubic shape composed of tiny blocks and flakes. EDX spectrum confirmed the elemental composition of Fe, Zn and O in the synthesized $ZnFe_2O_4$ nanoparticles. Thermo-gravimetric and differential thermal analysis (TG/DTA) method was used to confirm the formation of $ZnFe_2O_4$ nanoparticles. From the CV analysis, higher capacitance value observed for the lower scanning rate 2 mV/s. The electrochemical performance suggesting that the synthesized of $ZnFe_2O_4$ nanoparticles could be suitable for super capacitance application.
Keywords: *Nanoparticles, Co-precipitation technique, Cubic structure, Thermal, Supercapacitor.*

1. INTRODUCTION

In the recent years, environmental issues are at present the most important problem worldwide, and for that reason, there is an important demand for clean, efficient, and sustainable sources of energy as well as efficient technologies for energy storage [1, 2]. In this regard, supercapacitors have attracted increasing attention due to their long-life cycle, high power density, and ability to bridge the power/energy gap between batteries/fuel cells and traditional dielectric capacitors [3, 4]. The major challenge for the supercapacitor is the power density, the cyclic stability, and whether it can be cost-effective. Several researchers have been interested in the synthesis of new materials to meet the growing demand for electrochemical capacitors [5]. Moreover, supercapacitors and batteries are popular now electrochemical energy storage system in recent days. The batteries distribute high energy density and low power density whereas, conventional capacitors deliver high power density and low energy density. Supercapacitor is attractive because it can afford high power density, high-rate capability, and long cycle life [6, 7]. These supercapacitors have plentiful potential applications such as power electronics, electric vehicles, sensor, and computer backup etc., [8].

In literature, the metal oxides are too expensive for commercial purposes; however, the search for appropriate and cheap materials still continues. With this purpose in mind, iron oxides have been identified as a low-cost and potentially environmentally friendly material. Among the iron oxides, magnetite (Fe_2O_4) is considered as a supercapacitor material [2]. Indeed, spinel ferrites are competitive crystalline materials due to their excellent electrical properties. The structural equation of spinel ferrite is XFe_2O_4, where is a divalent metal ion. For the last few decades, many researchers studied the physical properties of ferrites substituting X with Co^{2+}, Ni^{2+}, Mg^{2+}, Zn^{2+} and Mn^{2+} [8, 10-14]. Among the divalent metal ions, zinc improves the efficiency of ferrites in many fields especially electrical storage system and photocatalysis [1, 13-16].

In this current work, we focus on the synthesis, electrical properties of zinc ferrites nanoparticles prepared by using a low cost and simple co-precipitation method for super-capacitor application. The zinc ferrites nanoparticles were characterized using X-ray diffraction (XRD) analysis, scanning electron microscope

(SEM), Fourier transform infrared spectroscopy (FTIR), Energy Dispersive X-ray Spectroscopy (EDX), Thermal analysis (TG/DTA) and Cyclic voltammetry (CV). These characterization techniques provided valuable information on the structural, morphological, electrochemical, thermal and chemical characteristics of the zinc ferrite nanoparticles.

2. Experimental

2.1 Synthesis of $ZnFe_2O_4$ nanoparticles

The precursor for the formation of $ZnFe_2O_4$ nanoparticles was prepared through a novel co-precipitation process, using $ZnFe_2O_4$ as the precipitant. All chemicals were sourced from Merck Chemicals. Firstly, $Zn(NO_3)_2{\cdot}6H_2O$, $Fe(NO_3)_2{\cdot}9H_2O$, and citric acid ($C_6H_8O_7$) were separately dissolved in 20 ml of deionized water. Sodium hydroxide (NaOH) was slowly added drop by drop to the mixture, which was stirred at 60 minutes for 80 ◦C. The presence of citric acid behaved as a chelating agent during the process, resulting in the development of brown-coloured precipitates. The precipitates were widely cleaned multiple times using deionized water and acetone. Subsequently, they were dried at 80 °C to obtain dark brown precipitates. Finally, the precipitates were subjected to calcinations at 500 °C for 3 h in a furnace.

2.2 Characterization techniques

The X-ray diffraction (XRD) analysis was examined to assess the crystalline phase of the $ZnFe_2O_4$ nanoparticles utilizing an instrument BRUKER USA D8 Advance, Davinci with CuKα radiation (λ = 1.54060 Å), operating at 40 kV and 30 mA. The characterization purposes, a scanning electron microscope (SEM) with EDX system from OXFORD Instrument have been performed Sigma 300 model was utilized after sputtering the sample and high-resolution transmission electron microscope, specifically the Jeol/JEM 2100, was utilized. Fourier transform infrared (FTIR) spectroscopy was performed using Purkin Elmer model Spectrum Two. The degradation behavior of the synthesized sample was assessed using a thermal gravimetric and differential thermal analysis (TG/DTA) conducted with a NETZSCH-STA 449 F3 JUPITER instrument. To assess the electrochemical properties, cyclic voltammetry (CV) was performed using a Versa STAT MC model.

3. RESULTS AND DISCUSSION

3.1 XRD analysis

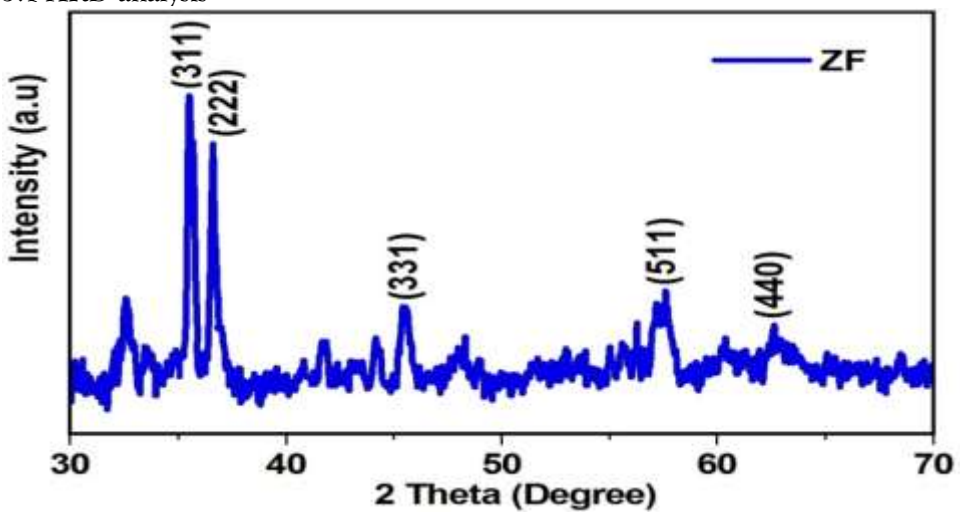

Figure 1 X-ray diffraction patterns of $ZnFe_2O_4$ nanoparticles

Fig. 1 shows the powder X-ray diffraction patterns for as-synthesized $ZnFe_2O_4$ nanoparticles annealed at 500°C prepared using the co-precipitation method. The XRD patterns of the $ZnFe_2O_4$ nano particles reveal the specific reflections (311), (222), (331), (511) and (440) corresponding to 2-theta angles of 35.32◦, 36.98◦, 41.92◦, 56.86◦, and 62.69◦, respectively, which are match with the characteristic of the Fd-3m cubic spinel structure (JCPDS Card no. 22-1012) [17]. The crystallite size (D) of the sample was calculated from the (311) peak using Scherrer's formula [18].

$$D = \frac{0.94\,\lambda}{\beta_D \cos\theta} \qquad \text{(1)}$$

Where β_D is the full width at half maximum (FWHM) of diffracting peak, λ is the wavelength of X-ray (0.1541 nm) and θ is the Bragg's diffraction angle. The crystallite sizes of the sintered $ZnFe_2O_4$ nano particles were in the range of 32 nm.

3.2 Structural analysis

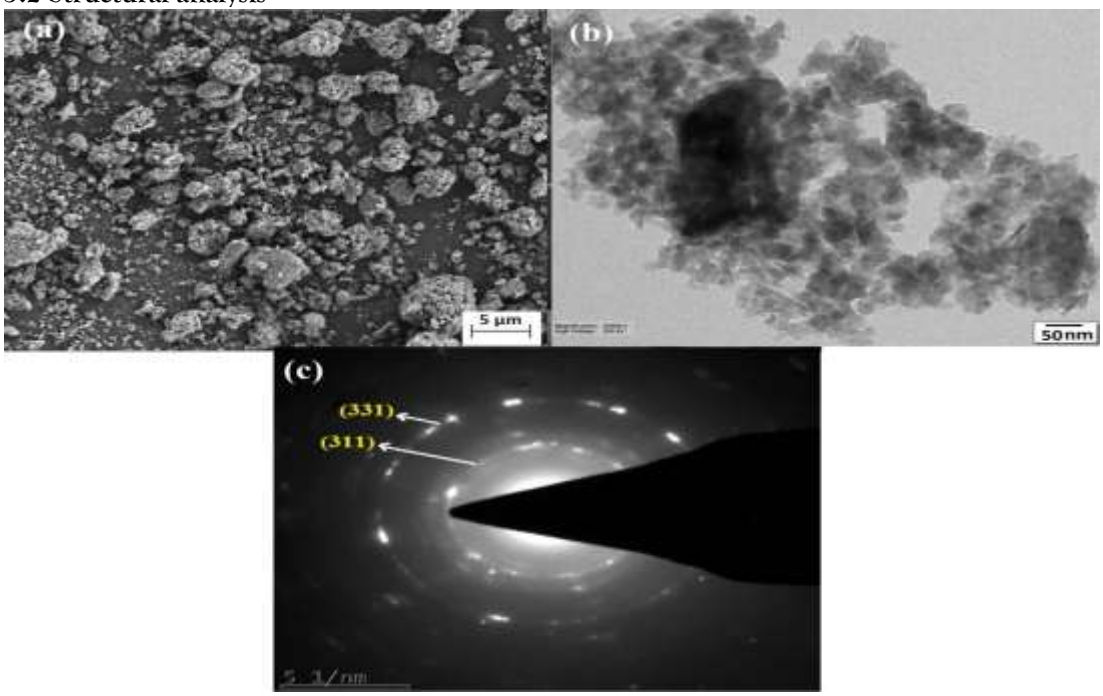

Fig. 2 (a) SEM image, (b) TEM image and (c) SAED pattern of $ZnFe_2O_4$ nanoparticles

The surface morphology of the synthesized $ZnFe_2O_4$ was examined, scanning electron microscope (SEM) and transmission electron microscope (TEM) images are depicted in Fig. 2 (a and b). The synthesized materials show an uneven surface morphology characterized by a quasi-cubic shape composed of tiny blocks and spheres. The environment of SEM micrograms is so typical to identify the shapes of the $ZnFe_2O_4$ nanoparticles. From the TEM results (figure 2 (b)), the formation of more small particles on the surface like spherical morphology, distributed uniformly on top of bigger blocks to create a rough surface. The observed increase in roughness on the surface of $ZnFe_2O_4$ nanoparticles has an impact on the electrochemical properties of the synthesized material since an electrochemical reaction takes place on the surface of the material [1]. The SAED pattern (Fig. 2(c)) reveals the presence of circular rings from the $ZnFe_2O_4$ cubic spinel structure and no additional rings are detected. The diffraction rings in the SAED pattern are in good agreement with the standard data (JCPDS Card no. 22-1012)) of $ZnFe_2O_4$.

3.3 Elemental composition analysis

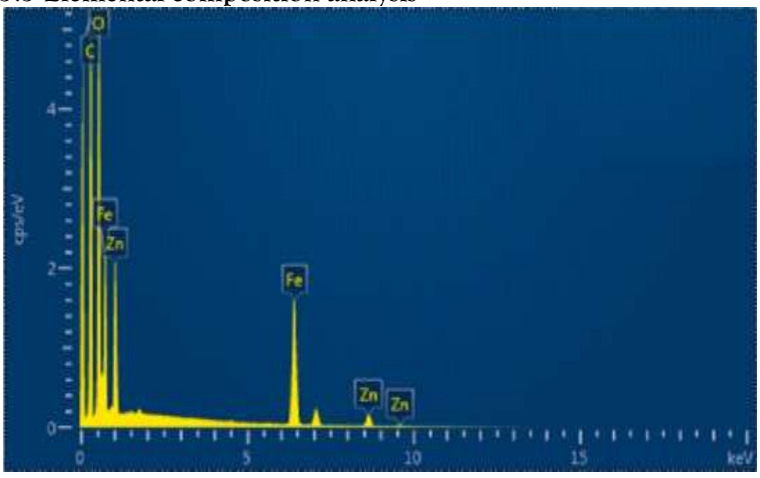

Fig. 3 EDX spectrum of $ZnFe_2O_4$ nanoparticles

Elemental composition analysis of $ZnFe_2O_4$ nano ferrite sample has been studied through the Energy Dispersive X-ray (EDX) spectrum. The characteristic EDX spectra of $ZnFe_2O_4$ nanoparticles are shown in Fig. 3, we can clearly observe presence of the constituent elements Fe, Zn, and O in the samples without impurities. The atomic peaks of iron (Fe), zinc (Zn), and oxygen (O) are identified. From the EDX results, O, Fe and Zn are found to have chemical compositions of 44.91 wt%, 34.87 wt%, and 10.22 wt% in the $ZnFe_2O_4$ nanoparticles, respectively. In addition, the atomic percentages (%) for O, Fe and Zn are found to be 31.72 %, 48.23 %, and 20.01 %, respectively. Small peaks were also found, which could be due to

the impurities from sample holder of the instrument [19]. Fig. 4 (a and b) shows the elemental mapping of the $ZnFe_2O_4$ nanoparticles. From the figure, the signals pertaining to Zn, Fe, and O have a uniform spatial distribution.

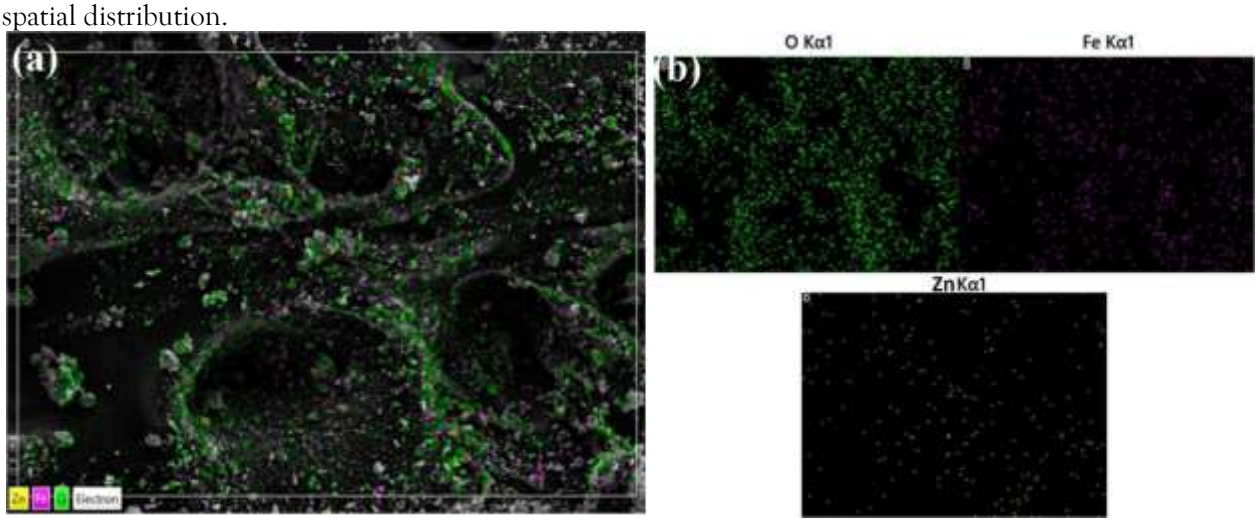

Fig. 4 (a and b) elemental composition images of $ZnFe_2O_4$ nanoparticles

3.4 FTIR-spectrum

Infrared (IR) transmittance spectrum of $ZnFe_2O_4$ nanoparticles was recorded in the wavenumber range 3000–500 cm^{-1} at room temperature. Figure 5 depicts the FTIR spectrum of $ZnFe_2O_4$ nanoparticles. The vibrational frequency around 600–500 cm^{-1} is related to the Fe^{3+} – O^{2-} complex at the tetrahedral site, proposed by Waldron et al. [20].

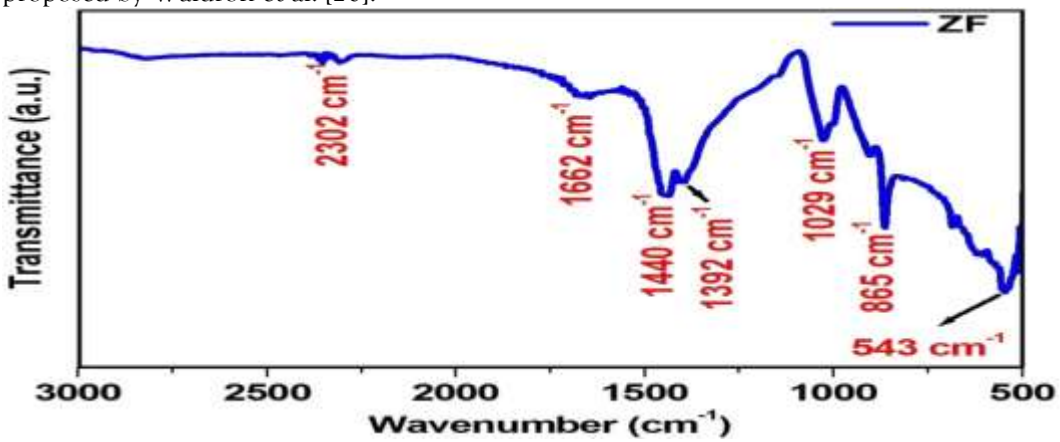

Figure 5 FTIR spectrums of $ZnFe_2O_4$ nanoparticles

The spectra showed characteristic peak of tetrahedral and octahedral Fe–O stretching band at 543 cm^{-1} [21]. V. A. Fabiani et al., [22] reported that the wavenumber 543 cm^{-1} corresponding to the vibrational mode of the metal oxygen bond (Zn-O-Fe). The C–O and C–N stretching bands at 1029 cm^{-1} indicate the presence of secondary alcohol and aromatic amine, respectively [23]. The bands corresponding to 3000 cm^{-1} and 1000 cm^{-1} represent stretching and bending vibrations of H–O–H, which indicates the presence of free or absorbed water in the samples [24]. In addition to these vibrational modes, a broad hump due to bending mode of water at 1662 cm-1 are observed in this spectrum. The broadness of stretching mode is attributed to the existence of weak hydrogen bonding [25]. The vibrational band at 2302 cm^{-1} is absorbed water molecules and allocated to the remained free in the $ZnFe_2O_4$ during the preparation [26]. Moreover, the peak at 2327 cm^{-1} reveals the O–H stretching vibration of the absorbed water molecule [27]. The symmetric and anti-symmetric stretching modes of carboxylate ions are obtained at 1440 and 1392 cm^{-1}. These peaks indicate the presence of oleic acid in these $ZnFe_2O_4$ nanoparticles.

3.5 Thermal analysis (TG/DTA)

Thermal stability of the synthesized $ZnFe_2O_4$ nanoparticles was examined by simultaneous TG and DTA measurement. The result was carried out from room temperature to 900 °C temperatures at a heating rate of 10°C/min which is shown in Fig.6. Three major weight losses have been found from TG analysis. The first stage of weight loss is observed at a temperature below 120 °C (11%) due to desorption of water. The second weight loss is predicted in the range from 120 °C to 175 °C (8%) as a result of decomposition

of organic templates. No weight loss is found between 175 °C and 680 °C indicating the formation of $ZnFe_2O_4$ nanoparticles. The third weight loss of (3%) is observed beyond 680 °C due to crystallization of the final product. Additionally, the exothermic peak in DTA curve at 190 °C due to the thermal decomposition of citric acid [28] which is associated in the formation of $ZnFe_2O_4$ nanoparticles.

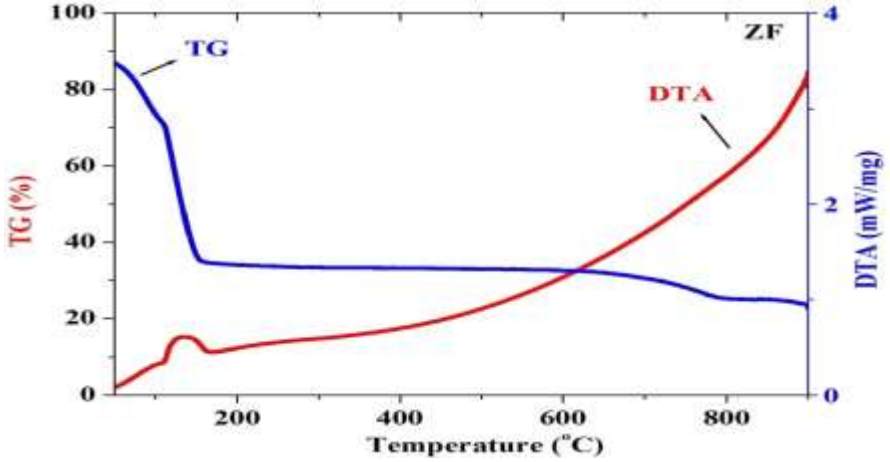

Fig. 6 TG/DTA curve of $ZnFe_2O_4$ nanoparticles

3.6 Cyclic Voltammetry

The electrochemical properties of $ZnFe_2O_4$ nanoparticles were confirmed from cyclic voltammetry (CV). Electrochemical measurements were performed at various scan rates (2, 5, and 1 0 mV s^{-1}) 1 in the 0 V and 0.6 V potential ranges as shown in Fig. 7. CV patterns are drawn between the current density versus applied potential under visible light irradiation. At lower scan rates, the CV curves display an ideal rectangular shape, indicative of well-defined capacitive behavior [29]. From the CV patterns of the $ZnFe_2O_4$ sample, which underwent calcination at 500 ◦C, reveal a pseudo-capacitive nature, as evidenced by changes in the CV curves with increasing scan rate. This indicates the presence of pseudo-capacitive processes within the system, indicating a dynamic capacitive response influenced by the scan rate. Moreover, these oxidation and reduction peaks have shifted to relatively higher and lower applied potentials with an increase in the scan rate [30]. The CV graphs of the $ZnFe_2O_4$ nanoparticles are nearly symmetrical with minor redox peaks, showing the pseudo-capacitive properties. The shapes of the CV curves do not change much, indicating their good electrochemical reversibility [31].

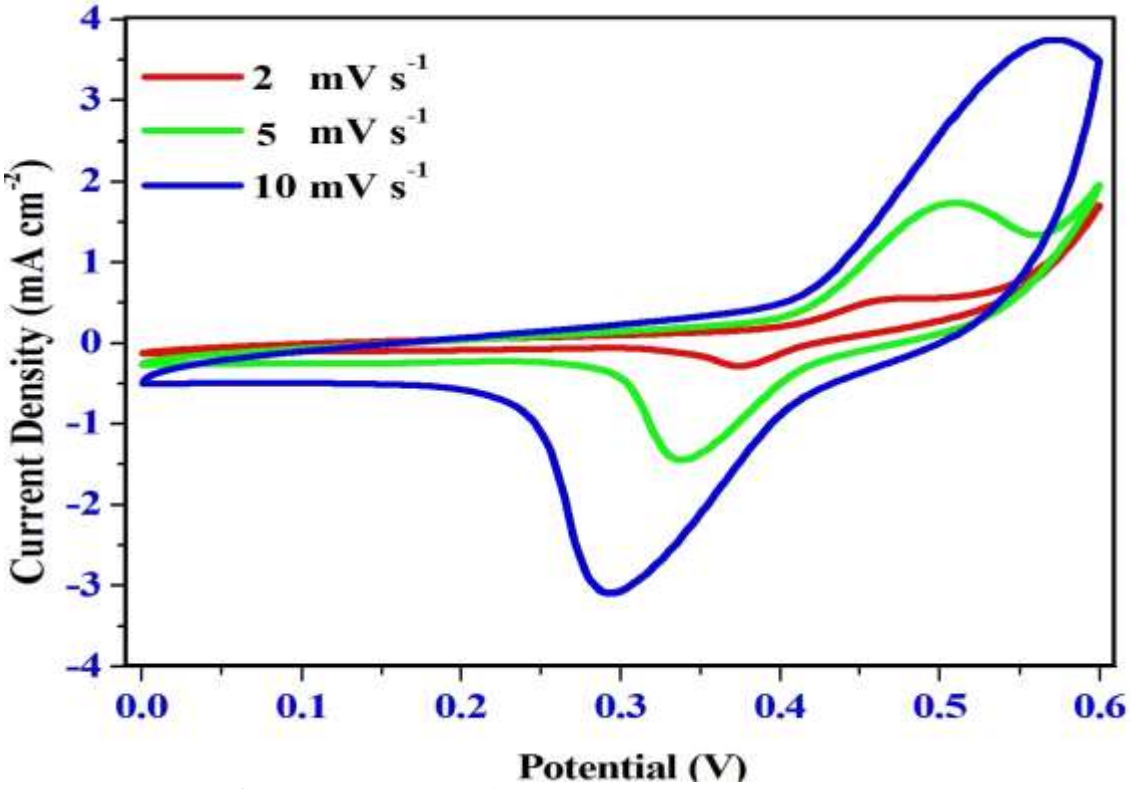

Fig. 7 CV pattern of $ZnFe_2O_4$ nanoparticles

The specific capacitances (Cs) value of the prepared $ZnFe_2O_4$ electrode was determined by using the following equation [32]

$$Cs = \frac{Q}{\Delta v.m} \qquad \text{(2)}$$

Here, Q stands for the anodic and cathodic charges that are measured during each cyclic voltammetry (CV) scan, and C_s is the electrode material's specific capacitance. The constant scan rate (mV s^{-1}) used for the measurements is indicated by Δv, whereas the variable m represents the mass of the active electrode material (in milligrams). Every CV analysis was carried out within the 0.0–0.6 V range.

The $ZnFeO_4$ CV profile's nearly perfect rectangular form indicates capacitive behaviour and is linked to faradaic redox processes that take place at the active electrode's surface. Additional proof of the electrode material's pseudocapacitive properties is provided by the existence of two separate redox peaks [33]. The oxidation and reduction peak current densities rise in tandem with the scan rate as it increases from low to high values, as illustrated in Fig. 9. Peak positions also somewhat shift [34]. Rapid and reversible redox reactions on the electrode surface because of this shift. Interestingly, the CV curves show good electrochemical reversibility, maintaining their shape without noticeable distortion, even at a relatively high scan rate of 10 mV s^{-1}.

One significant finding was that the specific capacitance was highest at the lowest scan rate. This suggests that electrolyte ions have enough time to penetrate the inner and outer surfaces of the porous electrode design at slower scan rates. Larger scan speeds, however, lead to less effective use of the electrode's active regions since ion transport is primarily restricted to the outer surface [35]. Better charge storage is made possible by $ZnFe_2O_4$'s high mesoporous nature, which seems to increase the active surface area.

Therefore, electric double-layer capacitance and faradaic redox contributions are both involved in the charge storage process, with the latter being more important because of the pseudocapacitive behavior. The electrode at 2 mV s^{-1} has the greatest capacitive double layer among the measured scan rates, suggesting efficient electron–hole separation and charge carrier transport at the electrode–electrolyte interface. For scan speeds of 2, 5, and 10 mV s^{-1}, the measured specific capacitance values are 221 Fg^{-1}, 151 Fg^{-1}, and 107 Fg^{-1}, respectively. For applications involving high-performance supercapacitors, this pattern shows that greater capacitance values can be obtained at lower scan rates, which is very beneficial.

4. CONCLUSION

In summary, $ZnFe_2O_4$ nanoparticles were successfully prepared by a simple, high yield and low-cost co-precipitation method. Structural, compositional and electrochemical properties of the synthesized $ZnFe_2O_4$ nanoparticles were well studied. XRD study reveals that the synthesized $ZnFe_2O_4$ nanoparticles were of phase pure with cubic structure. Morphological study of FESEM images reveals that the particles were in quasi-cubic shape composed of tiny blocks and flakes. EDX spectra confirmed the elemental composition of Fe, Zn and O in the synthesized $ZnFe_2O_4$ nanoparticles. FTIR confirmed the presence of zinc ferrite nanoparticles. No weight losses were noticed between 175 °C and 680 °C in TG and from 190 °C in DTA study confirmed the formation of $ZnFe_2O_4$ nanoparticles. The electrochemical performance of the $ZnFe_2O_4$ nanoparticles was investigated by CV analysis. The higher capacitance value was observed for the scanning rate 2 mV/s. The CV result reflecting the good quality of $ZnFe_2O_4$ nanoparticles possesses suitable for supercapacitor application.

REFERENCES

1. N. Masunga, O. J. Fakayode, B. B. Mamba and V. S. Vallabhapurapu, Through rare-earth doping, special attention was paid to improving the photo-electrochemical, optical, magnetic, and structural properties of zinc ferrite, Inorganic Chemistry Communications, 170 (2024) 113406-113414.
2. A. Chouchaine, S. Kouass, F. Touati, N. Amdouni and H. Dhaouadi, Fe3O4 nanomaterials: synthesis, optical and electrochemical properties, Journal of the Australian Ceramic Society, 57 (2021) 469–477.
3. J. Zhang, J. Jiang, H. Li and X. S. Zhao, A high-performance asymmetric supercapacitor fabricated with graphene-based electrodes, Energy Environmental Science. 4 (2011) 4009–4015.
4. W. Sugimoto, H. Iwata, Y. Yasunaga, Y. Murakami and Y. Takasu, Preparation of ruthenic acid nanosheets and utilization of its interlayer surface for electrochemical energy storage, Angewandte Chemie International Edition, 42 (2003) 4092–4096.
5. A. E. Fischer, K. A. Pettigrew, D. R. Rolison, R. M. Stroud and J. W. Long, Incorporation of homogeneous, nanoscale MnO2 within ultraporous carbon structures via self-limiting electroless deposition: implications for electrochemical capacitors, Nano Letters, 7 (2007) 281–286.

6. C. Liu, F. Li, L. P. Ma and H. M. Cheng, Advanced materials for energy storage, Advance Materials, 22 (2010) 28–62.
7. D. Chen, Q. Wang, R. Wang and G. Shen, Ternary oxide nanostructured materials for supercapacitors: a review, Journal of Materials Chemistry, 3 (2015) 10158- 10173.
8. P. Lavela and J. L. Tirado, CoFe2O4 and NiFe2O4 synthesized by sol–gel procedures for their use as anode materials for Li ion batteries, Journal of power sources, 172 (2007) 379- 387.
9. K. R. Prasad and N. Miura, Electrochemically synthesized MnO2-based mixed oxides for high performance redox supercapacitors, Electrochemistry Communications, 10 (2004) 1004-1008.
10. M. E. C. Ferreira, E. G. Bernardino, M. A. S. D. de Barros, R. Bergamasco, N. U. Yamaguchi, An overview of nanostructured manganese ferrite as a promising visible-light-driven photocatalyst for wastewater remediation, Journal of Water Process Engineering, 54 (2023) 104049-104016.
11. H. Ma, C. Liu, A mini-review of ferrites-based photocatalyst on application of hydrogen production, Front. Energy 15 (2021) 621–630, https://doi.org/10.1007/ S11708-021-0761-0/METRICS.
12. N. Masunga, O.K. Mmelesi, K.K. Kefeni, B.B. Mamba, Recent advances in copper ferrite nanoparticles and nanocomposites synthesis, magnetic properties and application in water treatment: review, J. Environ. Chem. Eng. 7 (2019) 103179,
13. J. Garg, M.N. Chiu, S. Krishnan, R. Kumar, M. Rifah, P. Ahlawat, N.K. Jha, K. K. Kesari, J. Ruokolainen, P.K. Gupta, Emerging trends in zinc ferrite nanoparticles for biomedical and environmental applications, Appl. Biochem. Biotechnol. 196 (2) (2023) 1008–1043.
14. S. N. Pund, P.A. Nagwade, A.V. Nagawade, S.R. Thopate, A.V. Bagade, Preparation techniques for zinc ferrites and their applications: a review, Mater. Today Proc. 60 (2022) 2194–2208.
15. A. Arimi, L. Megatif, L.I. Granone, R. Dillert and D.W. Bahnemann, Visible-light photocatalytic activity of zinc ferrites, Journal of Photochemistry and Photobiology, 366 (2018) 118–126.
16. J. Zhu, Y. Zhu, Z. Chen, S. Wu, X. Fang, Y. Yao, Progress in the preparation and modification of zinc ferrites used for the photocatalytic degradation of organic pollutants, International Journal of Environmental Research in Public Health, 19 (2022) 10710-10719.
17. W. Konicki, D. Siber and U. Narkiewicz, Removal of Rhodamine B from aqueous solution by ZnFe2O4 nanocomposite with magnetic separation performance, Polish Journal of Chemical Technology, 19 (2017) 65-74.
18. J. Samuel, T. S. F. Rajesh, C. S. Biju, S. S. J. Dhas and S. Usharani, Synthesis, structural, photoluminescence, ultraviolet blocking and antibacterial performances of Ba-doped ZnO nanostructures, Results in Optics, 12 (2023) 100482-100489.
19. J. Samuel, J. E. shaji, S. S. J. Dhas, S. Suresh, V. S. Vinita and C.S.Biju, UV-blocking performance and antibacterial activity of Cd, Ba co-doped ZnO nanomaterials prepared by a facile wet chemical method, Surface and Interface Analysis, 1 (2023) 1-14.
20. R. D. Waldron, Infrared spectra of ferrites, Physics Review, 99 (1955) 1727–1735.
21. G.S. Shahane, A. Kumar, M. Arora, R. P. Pant and K. Lal, Synthesis and characterization of Ni–Zn ferrite nanoparticles, Journal of Magnetism and Magnetic Materials, 322 (2010) 1015–1019.
22. V. A. Fabiani , H. Aldila, Anggraeni and Nuraini, Green synthesis and characterization of Zinc Ferrite (ZnFe2O4) nanocomposite via Tristaniopsis merguensis Griff. natural extract, Earth and Environmental Science, 599 (2020) 012066-012071.
23. A. Singh, N. B. Singh and K. Priya, Dose-dependent cytotoxicity against lung cancer cells via green synthesized $ZnFe_2O_4$/cellulose nanocomposites, e-Polymers, 23 (2023) 20230113-20230120.
24. M. Deepty, C. Srinivasa, E. R. Kumar, N. K. Mohan, C. L. Prajapate , T. V. Chandrasekhar Raoe , S. S. Meena , A. K. Verma and D. L. Sastry, XRD, EDX, FTIR and ESR spectroscopic studies of co-precipitated Mn–substituted Zn–ferrite nanoparticles, Ceramics International, 45 (2019) 8037–8044.
25. M. G. Naseri, M. H. M. Ara, E. B. Saion and A. H. Shaar, Super-paramagnetic magnesium ferrite nanoparticles fabricated by a simple, thermal-treatment method, J. Magnetism and Magnetic Materials, 350 (2014) 141–147.
26. L. A. Kafshgari, M. Ghorbani and A. Azizi, Synthesis and characterization of manganese ferrite nanostructure by co-precipitation, sol-gel, and hydrothermal methods, Particulate Science and Technology, 37 (2018) 904–910.
27. M. M. N. Ansari, S. Khan and N. Ahmad, Effect of R3+ (R= Pr, Nd, Eu and Gd) substitution on the structural, electrical, magnetic and optical properties of Mn-ferrite nanoparticles, Journal of Magnetism and Magnetic Materials, 465 (2018) 81–87.
28. P. Sivagurunathan and K. Sathiyamurthy, Effect of Temperatures on Structural, Morphological and Magnetic Properties of Zinc Ferrite Nanoparticles, Canadian Chemical Transactions, 4 (2016) 244-254.
29. D. Abisha, S. R. Gibin, V. K. PremKumar and A. Mariappan, Improved supercapacitor application of manganese ferrite nanoparticles via co-precipitation technique, Heliyon, 9 (2023) 21120-21131.
30. L. A. Kafshgari, M. Ghorbani and A. Azizi, Synthesis and characterization of manganese ferrite nanostructure by co-precipitation, sol-gel, and hydrothermal methods, Particulate Scientific. Technology, 37 (2018) 904–910.
31. G. Nabi, K. N. Riaz , M. Nazir, W. Raza, M. B. Tahir, M. Rafique, N. Malik, A. Siddiqa, S. S. Ali Gillani, M. Rizwan, M. Shakil and M. Tanveer, Cogent synergic effect of TiS2/g-C3N4 composite with enhanced electrochemical performance for supercapacitor. Ceramics International, 46 (2020) 27601-27607.
32. S. C. Pang, B. H. Wee and S. F. Chin, The capacitive behaviors of manganese dioxide thin-film electrochemical capacitor prototypes, International Journal of Electrochemistry, 2011 (2011).
33. K. Sathishkumar, N. Shanmugam, N. Kannadasan, S. Cholan and G. Viruthagiri, Opto, magnetic and electrochemical characterization of Ni1− xCoxO nanocrystals, Journal of Materials Science: Materials in Electronics, 26 (2015) 1881–1889.
34. D. Toloman, A. Gungor, A. Popa, M. Stefan , S. Macavei, L. B. Tudoran, A. Varada, I. Deniz Yildirim, R. Suciu, I. Nesterovschi, M. Mihet, E. Erdem and A. M. Rostas, Morphological impact on the supercapacitive performance of nanostructured ZnO electrodes, Ceramics International, 51 (2025) 353–365.
35. N. Kitchamsetti, Y. R. Ma, P. M. Shirage and R. S. Devan, Mesoporous perovskite of interlocked nickel titanate nanoparticles for efficient electrochemical supercapacitor electrode, Journal of Alloys and Compounds, 833 (2020) 155134-155147.